CHAPTER V

Performance Improvement[††]

Chapter index

[††] Part of this work has been submitted to *Journal of EM Waves and Applications*, S. Shee, and S. Dwivedi, "Design and simulation study of double side-cavity grid-less reltron with dual extraction sections,"

CHAPTER 5

Performance Improvement

5.1 Introduction

Reltrons have undergone extensive theoretical and experimental development for more than two decades. As a result, the early single-shot, fixed-frequency designs have evolved into long-pulse, high pulse repetition frequency (PRF), and tunable tubes covering 0.7-12 GHz. The versatile megawatt-class HPM oscillators have numerous advantages over other microwave tubes like – stable operating frequency, variable pulse duration, and a long maintenance-free lifetime of up to 10^5 pulses. A 20 MW L-band reltron tube, with a pulse duration of 5 μS and a PRF of 100 Hz, is about half a meter long and weighs less than 40 kg, including the focusing magnets [Miller *et al.* (1994)].

In the present chapter, computer-aided design and simulation-based study have been carried out on a double side-cavity (DSC) grid-less reltron with a dual extraction section, and the improvement in performance is reported. Beam-absent, beam-present, and electrostatic simulations are performed. In addition to the three normal modes in a conventional reltron, an extra mode (pseudo $\pi/2$ mode) is identified in the DSC reltron. Further investigation shows that this mode does not affect the device performance. The performance chart of the proposed device has been obtained in terms of output power and efficiency.

5.2 Design of the DSC Reltron's Modulation Section

The design and working principle of DSC reltron are the same as conventional reltron, with three pillbox cavities. The dominant mode in a pillbox is TM_{010}. The operating frequency is the primary parameter for designing the modulation section. The radius of the two on-axis cavities (first and second cavity) (r_mc) is calculated from eqn. 2.1. Two side-cavities are connected across the main cavity in a DSC reltron. The side cavities and idler discs are designed using eqn. 2.2, 2.3, and 2.4. The first and the second cavity is magnetically coupled through the two side cavities (Figure 5.1). An electrical coupling

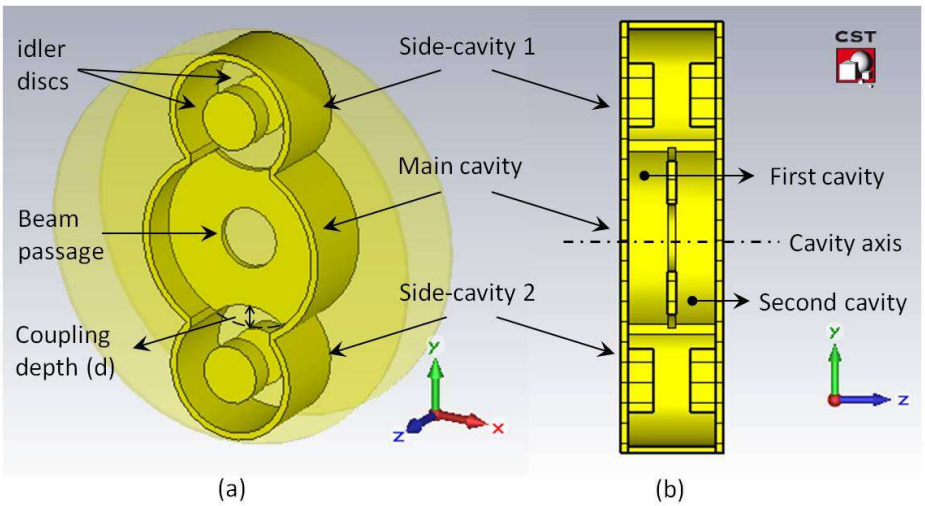

Figure 5.1: The modulation section of a DSC reltron. (a) Perspective view (cavity side-walls are made transparent for a better view) and, (b) cross-sectional view.

also exists between the two through the circular beam passage at the cavity axis (Figure 5.1(a)). But it happens at a frequency, which is well above the operating frequency. The modulation section should be designed by adding a margin of $\sim$2% to the desired operating frequency, since the resonant frequency shifts in a coupled multi-cavity structure. The beam loading also causes a minor reduction in the operation frequency [Gilmore (2001)]. The cavity dimensions are listed in Table 5.1.

From the cross-sectional view of the modulation section (Figure 5.1 (b)), it appears as if there is a single annular side-cavity with annular idler discs, which can be misleading.

Table 5.1: Dimensions of the modulation section.

List of parameters	Values (mm)
Radius of main cavity (r_mc)	38.5
Length of main cavity (l_mc)	34
Radius of Side cavity (r_sc)	25.5
Length of side cavity 1, and 2 (l_sc)	34
Radius of Idler disc (r_idl)	12.5
Length of Idler disc (l_idl)	10
Grid thickness (t)	2
Coupling depth (d)	12

5.3 Beam-absent (Cold) Simulation and Results

Before going for the beam-present (hot) simulation, the normal modes and the S-parameters of an S-band DSC reltron's modulation section have been obtained. These are primary and structure-dependent quantities that govern the oscillation frequency and device operation.

5.3.1 Normal modes of DSC reltron

The mode designations and normal modes in conventional reltron have been discusses in section 2.5 and 3.3, respectively. The modes are designated depending on the phase difference of EM fields in the consecutive cavities, and their frequencies systematically depend on cavity dimensions. A DSC reltron's modulation section has been modeled in CST MWS and simulated with the AKS method to find the lowest order eigenmodes. In conventional reltron, there are three lowest order modes – 0, $\pi/2$, and π, in the increasing order of frequency [Miller *et al.* (1992)].

As there are four cavities in DSC reltron, four normal modes appear here. The vector plot and the contour plot of all normal modes are shown in Figure 5.2 and Figure 5.3, respectively. The frequency of the new mode lies in between the first three modes. In this mode, the instantaneous phase differences among the electric fields in the consecutive cavities are $\pi/2$ radians but, the maximum electric field intensity occurs in the two side

cavities (Figure 5.2 (c) and Figure 5.3 (c)), unlike the main cavity in $\pi/2$ mode (Figure 5.2 (b) and Figure 5.3(b)). This mode is designated as the pseudo-$\pi/2$ mode. There

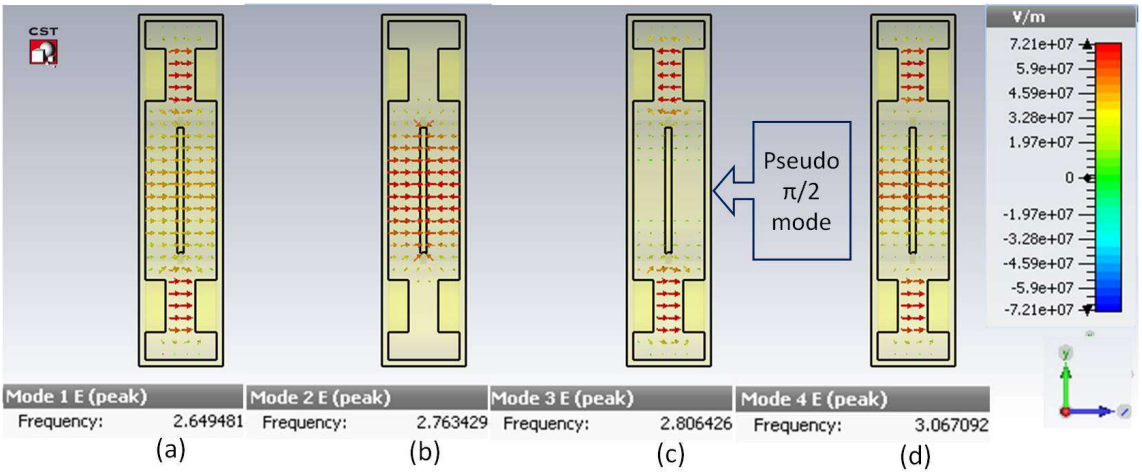

Figure 5.2: A cross-sectional view of the modulation section of a DSC reltron showing vector plots of (a) mode 0: 2.649481 GHz, (b) mode $\pi/2$: 2.763429 GHz, (c) mode pseudo-$\pi/2$: 2.806426 GHz and, (d) mode π: 3.067092 GHz, respectively.

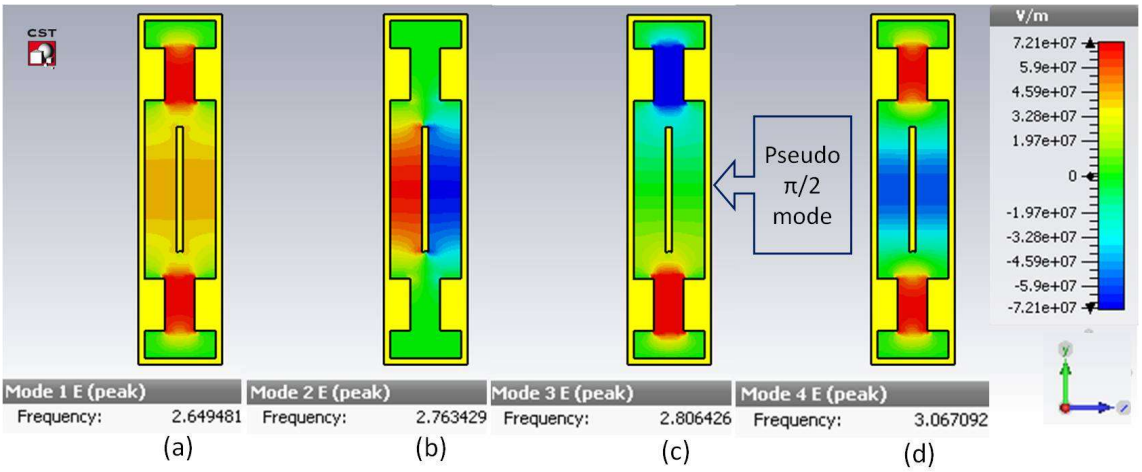

Figure 5.3: A cross-sectional view of the modulation section of a DSC reltron showing contour plots of (a) mode 0: 2.649481 GHz, (b) mode $\pi/2$: 2.763429 GHz, (c) mode pseudo-$\pi/2$: 2.806426 GHz and, (d) mode π: 3.067092 GHz, respectively.

is no electric field at the cavity axis and minimum intensity at its surrounding. So, it is presumable that the pseudo-$\pi/2$ mode does not modulate the beam's velocity and hence, does not affect the device performance. This has also been confirmed from the output signal spectrum obtained through PIC simulation in the next section.

5.3.2 S-parameter

The S-parameter of the modulation section has been obtained using the general-purpose broadband frequency sweep method of the Frequency-domain solver discussed in Chapter 2 (subsection 2.7.1), as well as the Transient solver with adaptive hexahedral mesh refinement discussed below.

Transient solver and Adaptive Mesh Refinement: This solver is a finite integration technique (FIT) [Clemens *et al.* (2001)] based solver that allows precise modeling of small and curved structures without the extreme refinement of the mesh. So, it is memory efficient in simulating extremely complex structures. This solver is less efficient for structures that are much smaller than the shortest wavelength under consideration. The adaptive mesh refinement creates a denser mesh for a given structure. The initial meshing is generated by an expert system and is used in the first pass. The expert system based refinement strategy successively changes the mesh settings until a specified S-parameter convergence criterion is attained, and appropriate mesh is obtained. These settings are used afterward for further parameter studies without activating the adaptive meshing again. The minimum and the maximum number of passes can be specified in the mesh refinement settings. The minimum number of passes is performed even if there is no significant change in S-parameter. The maximum number of passes helps in limiting the total simulation time to reasonable amounts. The lines per wavelength define the minimum number of mesh lines to be used in each coordinate direction for this length. This setting has a strong influence on the quality of the results and on the calculation time. Increasing this number leads to higher accuracy and increased simulation time. A good compromise between simulation time and accuracy is achieved at the default value of 10. When an S-parameter is simulated using time signals that still show some oscillation, a ripple appears on the S-parameters. However, the positions of the resonance frequencies are not affected by the ripple. Auto regressive (AR) filters are capable of calculating the frequency spectra for time signals, which have not reached a steady state. In this technique, an AR filter is first trained using a short interval of the time signals and then used to predict the signal for next steps. Once the prediction matches the actual simulation, the

AR-filter acquires all relevant information about the device. Thereafter the S-parameters can be mathematically derived from the filter's representation.

Standard flange-mount SMA connectors with exposed TFE (tetrafluoroethylene) were modeled at both ends of the main cavity along the axis. Waveguide ports were defined on the dielectric region of the SMA connector to excite the structure, as before. Figure 5.4 (a) and (b) shows the simulated S-parameter obtained from the Frequency-domain and the Transient solver, respectively. The three distinct indicates the frequency selective, and resonant behavior of the modulation section. Table 5.2 compares the normal mode

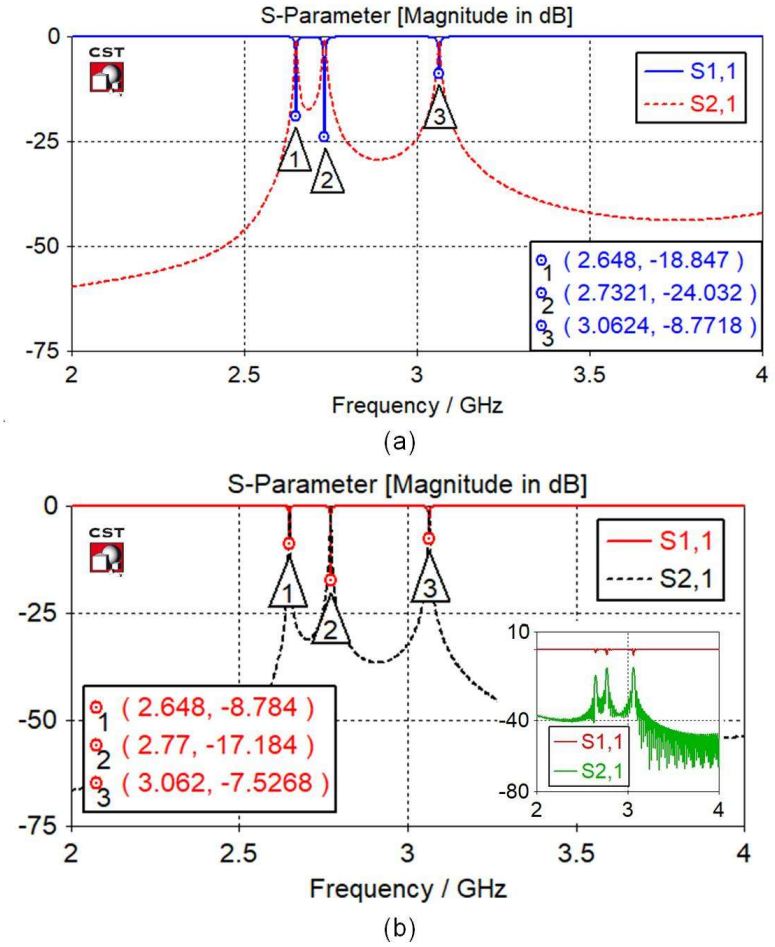

Figure 5.4: Simulated S-parameter of DSC reltron modulation section from (a) Frequency-domain solver, and (b) Transient solver (inset: without AR-filtering). Marker 1, 2, and 3 correspond to 0, $\pi/2$, and π mode, respectively.

frequencies from the Eigenmode solver, and S-parameter minima from the Frequency-domain solver, and Transient solver. Transient solver has attained a closer match with the Eigenmode solver results, in all three frequencies.

Table 5.2: Comparison among frequencies (GHz) of normal modes (Eigenmode solver) and S-parameter minima from Freq. domain (F.D.) solver, and Transient (T.D.) solver

Mode designation	Normal mode freq.	S_{11} min F.D.	S_{11} min T.D.	Diff. F.D.(%)	Diff. T.D.(%)
0	2.649481	2.6480	2.648	0.06	0.06
$\pi/2$	2.763429	2.7321	2.770	1.13	0.24
π	3.067092	3.0624	3.062	0.15	0.15

5.4 Beam-present (Hot) Simulation and Results

After the cold simulations of the modulation section, a systematic exploration of the DSC reltron is performed through beam present PIC simulation.

A conventional (single side cavity) S-band grid-less reltron with, and specifications listed in Table 5.3 has been modeled first. Explosive emission type stainless steel cathode is

Table 5.3: Parameters and dimensions used in PIC simulation

List of parameters/materials	Values
Cathode voltage	100 kV
Postacceleration voltage	100, 200, 300,and 400 kV
Rise time of input signal	10 nS
Anode cathode gap	17 mm
Postacceleration gap	45 mm
Predefined magnetic field	0.2 T
Extraction section	WR284 (72.14×34.04 mm)

used, and similar simulation setup is arranged for supplying the cathode and the postacceleration potentials, and recording the output. The modeling of the extraction section is also similar. The only difference is the annular disk, in place of highly transparent grid in the gridded reltron. The reference output power and efficiency for given cathode and postacceleration potential were achieved using the PIC solver. Thereafter the second side-cavity is added across the main cavity to modify the modulation section to the DSC type (Figure 5.5). Now, the postacceleration potential was increased through parametric

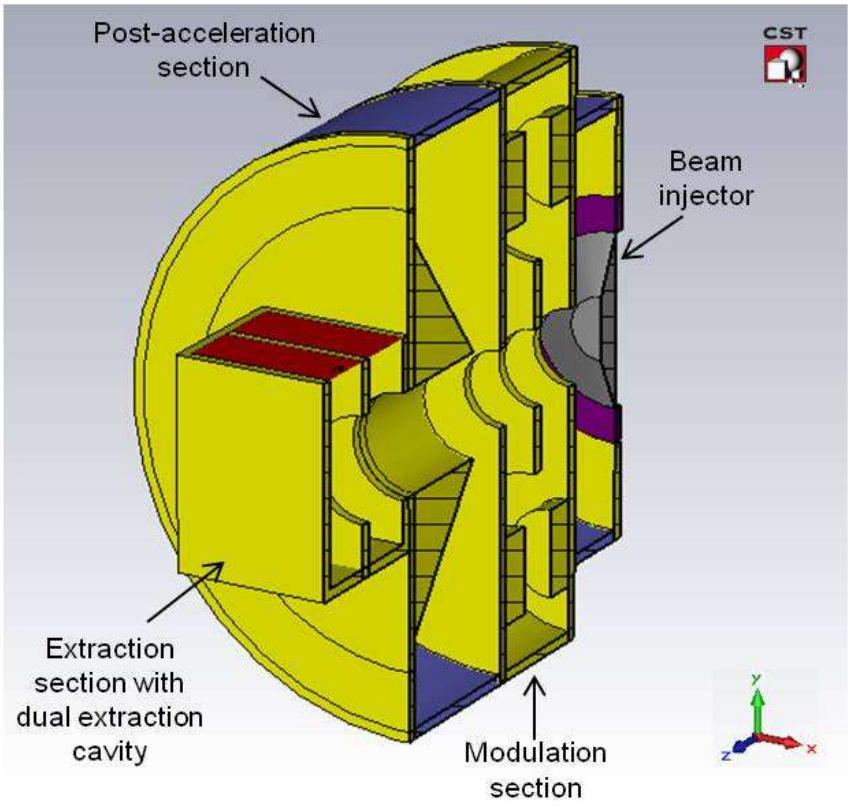

Figure 5.5: The cross-sectional view of a DSC grid-less reltron with dual extraction cavity.

sweep in the step of an integer multiple of the cathode potential, and the output power and the efficiency were recorded to construct a performance table.

5.5 Results and Discussions

The port signals and its first harmonics are shown in Figure 5.6 (a) and (b), at a fixed cathode potential of 100 kV and different postacceleration potentials. The corresponding spectrum are shown in Figure 5.7. The output power and efficiency were calculated in the respective cases and summarized in Table 5.4. At a fixed cathode potential, gradual increase in current is observed with increasing postacceleration potential. This would be possible if the beam current increase due to increased electric field at the anode-cathode (AK) gap. To investigate this possibility, the Electrostatic solver is used to obtain the static electric field inside the whole structure. This solver supports various source types like - fixed or floating potentials, field gradings, boundary potentials, charges on PEC (perfect electric conductors), and homogeneous volume or surface charge distributions.

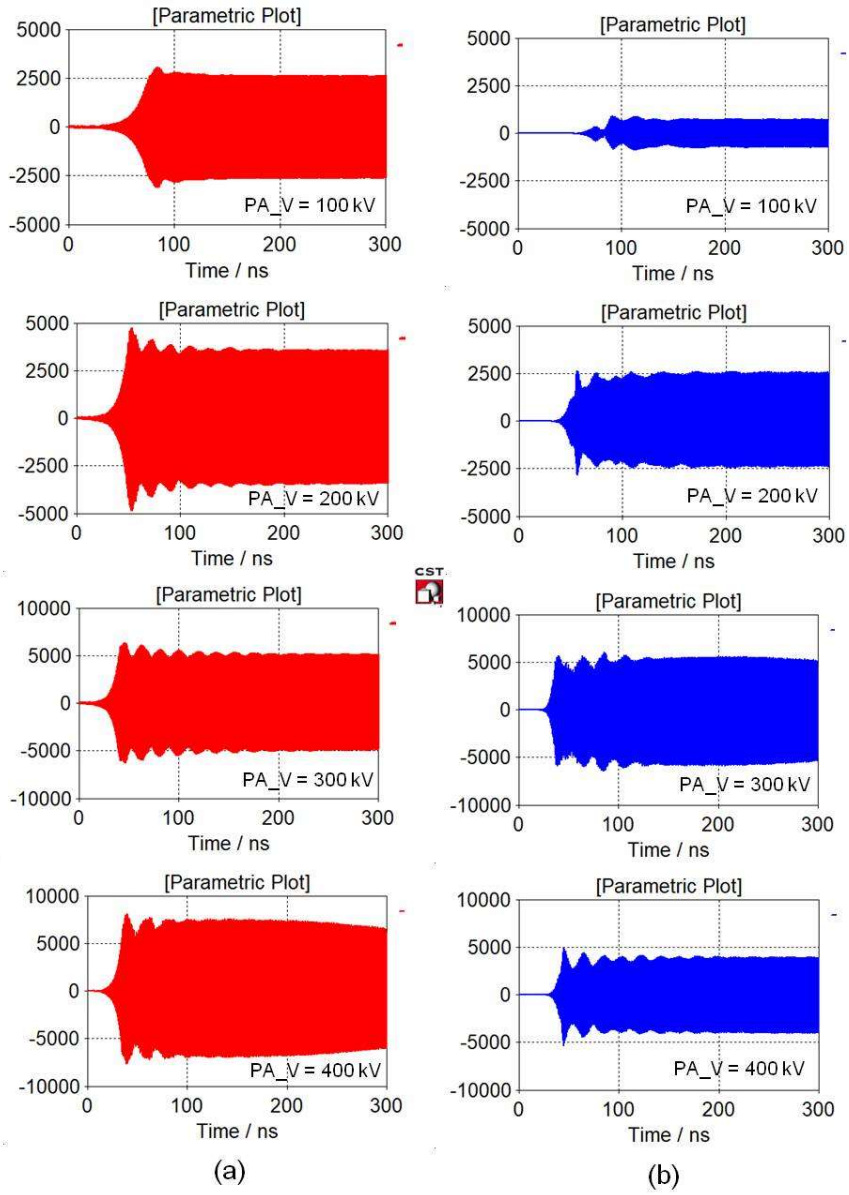

Figure 5.6: (a) Port signals ($\sqrt{W}$) from one of the extraction cavity for fixed cathode potential of 100 kV, (b) the corresponding first harmonics.

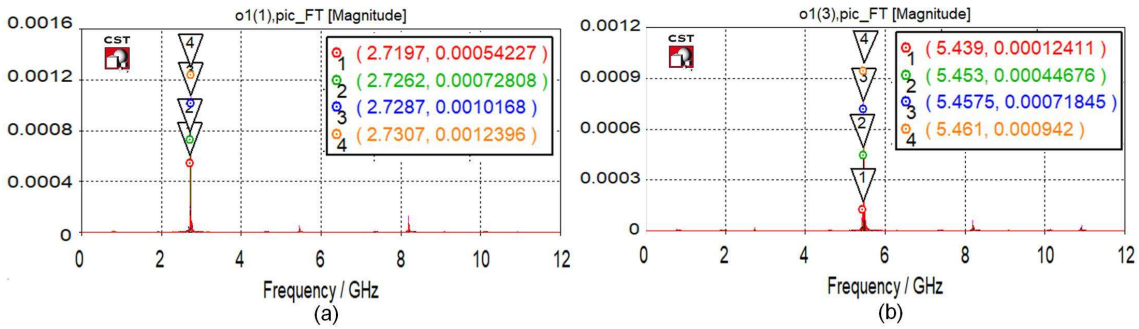

Figure 5.7: Spectrum of the port signals in (a) fundamental mode, and (b) first harmonics. Data markers indicate the frequencies (GHz) and corresponding amplitudes (V/m/GHz).

Table 5.4: Estimation of output power and efficiency.

Cathode potential (kV)	PA potential (kV)	Current (A)	Output power (MW)	Efficiency (%)
100	100	335	13.52	20.18
	200	415	25.78	31.06
	300	485	53.05	36.46
	400	700	108.05	38.59
	500	725	114.61	31.62
200	200	860	69.62	20.24
	400	940	128.00	34.04
	600	1075	129.61	20.09
	800	1075	114.85	13.35
	1000	1075	119.51	11.12

The electrostatic simulation is set up by assigning fixed electric potentials to the cathode, modulation section and, the postacceleration section after removing the particle and signal sources. The material is also changed to PEC. The electrostatic field contour at cathode and postacceleration potential of 200 kV and 400 kV are shown in Figure 5.8 (a) and (b), respectively. It shows a substantial increase in the static electric field at the AK-gap with

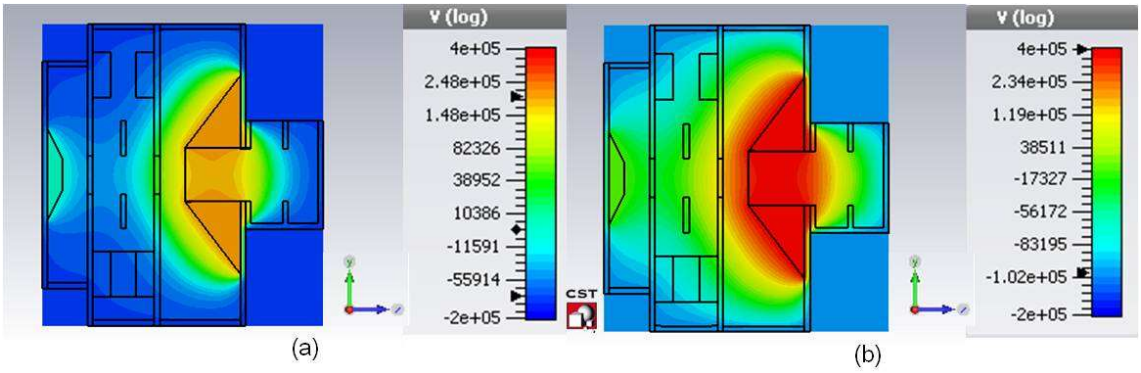

Figure 5.8: Contour plot of electrostatic potential for cathode potential of 100 kV and PA potential of (a) 200 kV and (b) 400 kV respectively.

an increase in postacceleration potential. As a result of this increased electric field, more current must have been emitted from the explosive emission cathode. This concludes that the increase in beam current with the postacceleration potential is due to the raised static electric field at the AK-gap. Table 5.4 also reveals that higher postacceleration potential causes a reduction in efficiency, with a relatively small increase in the output power. The reduction in efficiency is due to the difficulty in beam bunching at relativistic velocities

[Miller *et al.* (1992)].

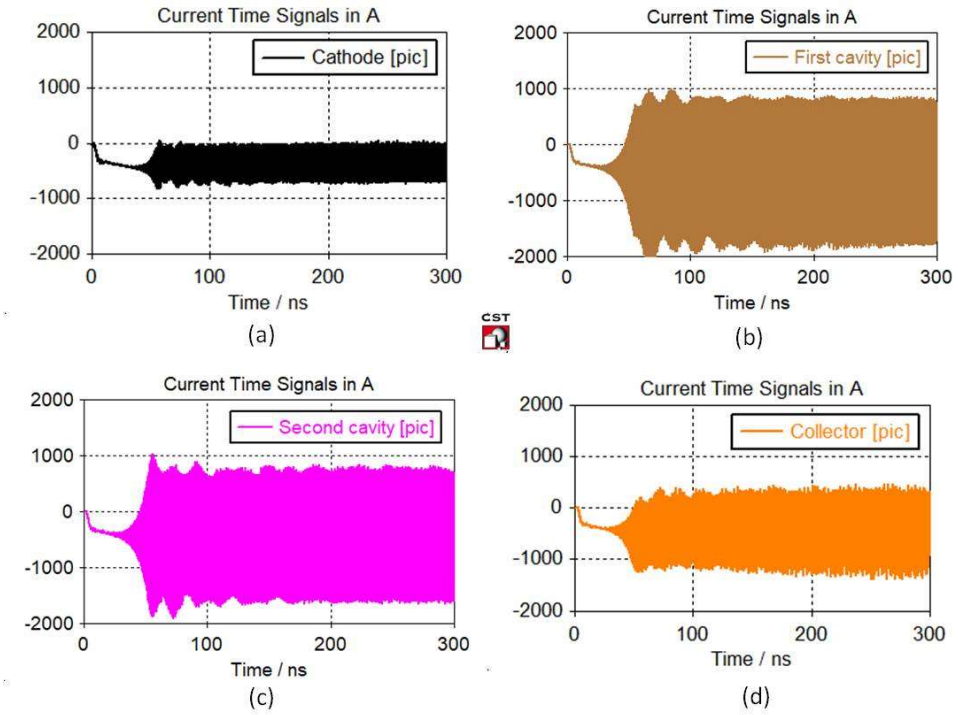

Figure 5.9: Temporal current (Amp) at (a) cathode, (b) first cavity, (c) second cavity and, (d) collector

The results of current monitors are shown in Figure 5.9. The phase space plot of normalized momentum at cathode potential of 100 kV and postacceleration potential of 200 kV is shown in Figure 5.10 (a) and (b). A comparison between fundamental mode port signals of a conventional reltron and a DSC reltron is shown in Figure 5.11. This shows about 25% increase in pulse the duration than the conventional reltron by a faster build up of oscillation. The longer pulse duration raises the energy per pulse, which increases the damage to electronics equipment in DEW applications.

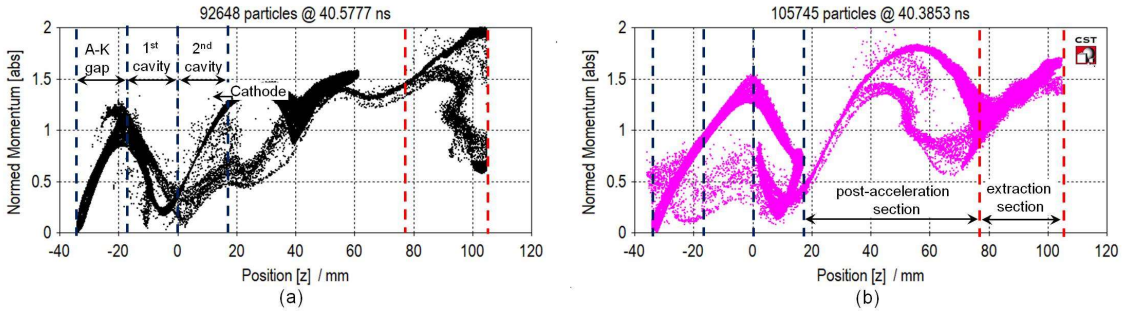

Figure 5.10: Phase space plot in two opposite cycles of the RF oscillation.

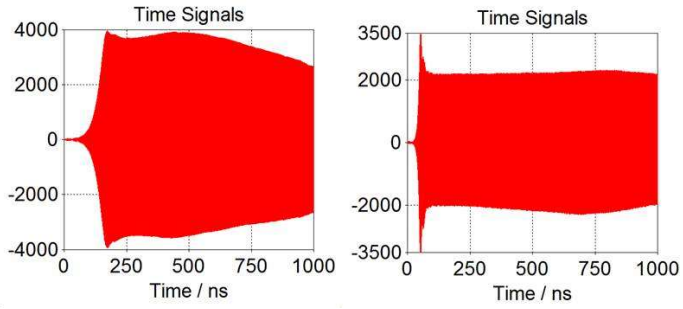

(a) (b)

Figure 5.11: Temporal field amplitude of fundamental mode of – (a) conventional, and (b) double side-cavity reltron.

5.6 Conclusion

Observations from the cold and hot simulations conclude the following–

Four normal modes appear in a DSC reltron modulation section, as it is comprised of four cavities. The Eigenmode solver has successfully captured all four modes. The pseudo $\pi/2$ mode has zero electric field at the cavity axis and minimum at its surroundings. Hence, it does not interfere in the beam wave interaction process. The operating frequency is found to be closest to that of $\pi/2$ mode. This confirms the $\pi/2$ mode operation. Also, the spectrum does not show any evidence of mode hopping or frequency chirping. However, the operating frequency is $\sim$43 MHz lower than the $\pi/2$ mode frequency that shows the effect of beam loading, which is common in all vacuum electron devices. The efficiency of the DSC reltron without applied postacceleration potential is found to be 20%, which is the same as the conventional reltron experiments. This validates the simulation model. The reduction in efficiency at a higher applied postacceleration potential (Table 5.4) might be due to the difficulty in beam bunching at relativistic velocities. The increase in beam current with the postacceleration potential is due to the raised static electric field at the AK-gap. A significant amount of power has been contained by the second harmonics (Figure 5.6 (b)), which would increase the effectiveness of reltron as a DEW. More than two cavities can be used for microwave extraction. However, the phase difference between the respective port signals becomes considerable when more than two consecutive cavities are considered, resulting in reduced output power.

CHAPTER vi

Summary, Conclusion and Future scope

Chapter index